

Large interfacial Rashba interaction generating strong spin-orbit torques in atomically thin metallic heterostructures

Supplementary Information

Sachin Krishna,¹ Yanis Sassi,¹ Fernando Ajejas,^{1,*} Nicolas Sebe,¹ Nicolas Reyren,¹
 Sophie Collin,¹ Thibaud Denneulin,² András Kovács,² Rafal E. Dunin-Borkowski,²
 Albert Fert,¹ Jean-Marie George,¹ Vincent Cros,^{1,†} and Henri Jaffrès^{1,‡}

¹*Unité Mixte de Physique, CNRS, Thales, Université Paris-Saclay, 91767, Palaiseau, France*

²*Ernst Ruska-Centre for Microscopy and Spectroscopy with Electrons (ER-C 1) and Peter Grünberg Institut (PGI-5),
 Forschungszentrum Jülich GmbH, 52425 Jülich, Germany*

I. HARMONIC HALL VOLTAGE MEASUREMENT TECHNIQUE TO EXTRACT SPIN-ORBIT TORQUES (SOTS).

Harmonic Hall voltage measurement technique has been used to determine quantitatively the two components of the SO torques (SOT) in our sample series. The measurement geometry is shown in Fig. S1. The Hall voltage (V_H) in a perpendicularly magnetized system is expressed as:

$$V_H = (R_0 + R_{AHE} \cos(\theta) + R_{PHE} \sin^2(\theta) \sin(2\phi)) I \quad (1)$$

where θ and ϕ are the polar and azimuthal angle of the magnetization, R_{AHE} is the anomalous Hall resistance, R_{PHE} is the planar Hall resistance and R_0 is the $x-y$ resistance arises due to imperfect device geometry. When an AC current of frequency f is injected in the Hall bar, it generates effective SOT fields (ΔH) that produces magnetic oscillations around its equilibrium ($\Delta\theta$, $\Delta\phi$). These oscillations modulate the Hall voltage in synchronization with current frequency f . By replacing $I \rightarrow I_0 \sin(2\pi ft)$, $\Delta H \rightarrow \Delta H \sin(2\pi ft)$, $\theta \rightarrow \theta + \Delta\theta \sin(2\pi ft)$, and $\phi \rightarrow \phi + \Delta\phi \sin(2\pi ft)$, we obtain the following expression for the measured Hall voltage:

$$V_H = V_0 + V_f \sin(2\pi ft) + V_{2f} \cos(4\pi ft) \quad (2)$$

with

$$V_f = (R_0 + R_{AHE} \cos(\theta) + R_{PHE} \sin^2(\theta) \sin(2\phi)) I_0 \quad (3)$$

and

$$V_0 = V_{2f} = 1/2 (R_{AHE} \sin(\theta) - R_{PHE} \sin(2\theta) \sin(2\phi)) \Delta\theta I_0 - R_{PHE} \sin^2(\theta) \cos(2\phi) \Delta\phi I_0 \quad (4)$$

Note that the V_f gives the information of magnetization direction (θ and ϕ) in the presence of an external magnetic field. Whereas, the V_{2f} contains all the information of magnetization oscillations ($\Delta\theta$, $\Delta\phi$) generated by the two torques. To extract the SOT effective fields, we simultaneously measure V_f and V_{2f} as a function of in-plane magnetic fields applied along the current direction in damping-like (DL) geometry and transverse to the current direction in field-like (FL) geometry (see Fig. S1). Note that the external magnetic field is applied slightly off-plane with an angle $\delta\theta_H \approx 7^\circ$ to ensure uniform magnetization inside the Hall bar.

For DL geometry, *i.e.*, $\theta_H = \pi/2 + \delta\theta_H$ and $\phi = \phi_H = 0$, after having replaced the values of $\Delta\theta$ and $\Delta\phi$, one obtains in the damping-like (DL) geometry, $H \parallel I$:

* Current address: Department of Physics and Center for Advanced Nanoscience, University of California, San Diego La Jolla, CA, 92093, USA.

† vincent.cros@cnrs-thales.fr

‡ henri.jaffres@cnrs-thales.fr

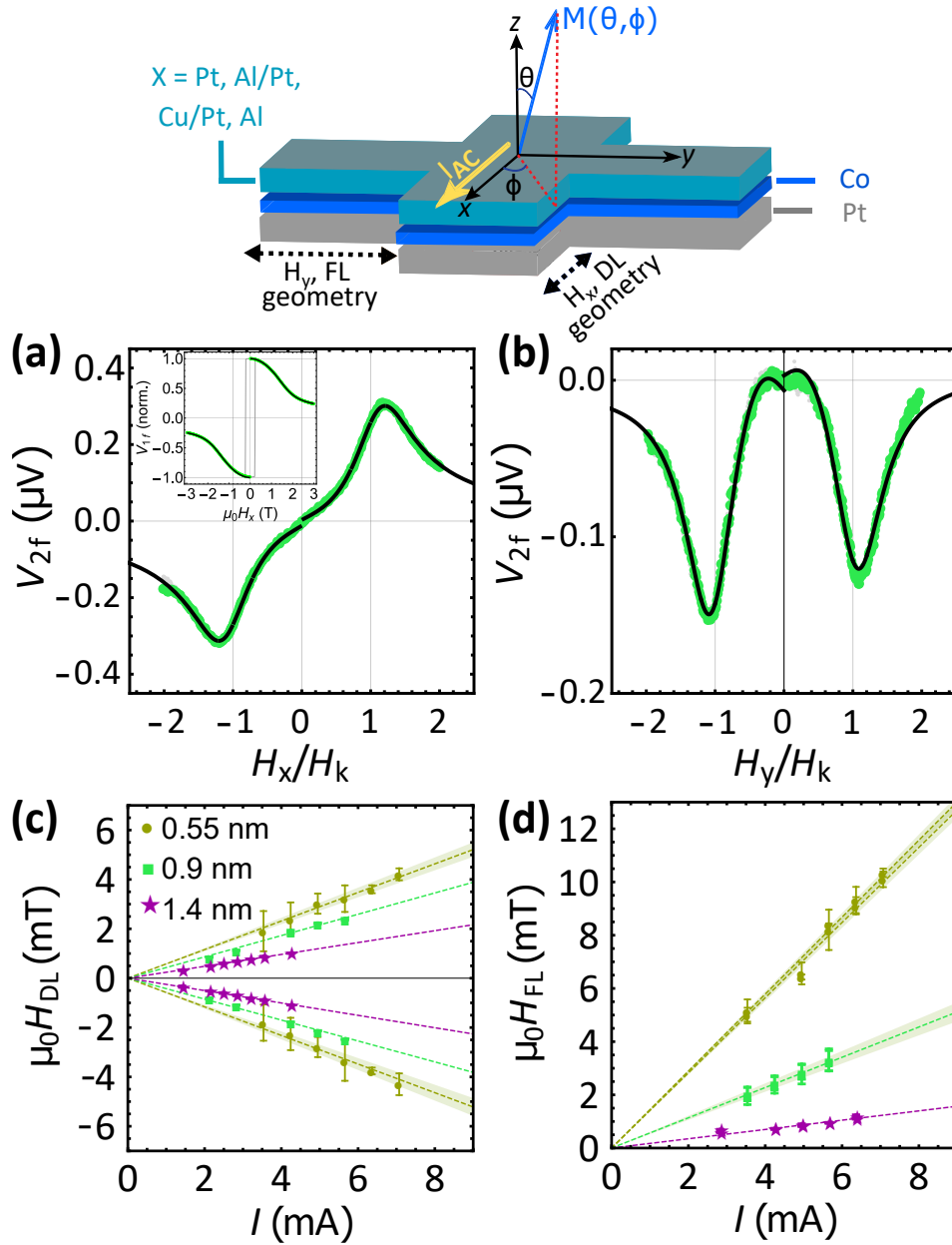


Figure S1. Harmonic Hall measurements of damping-like (DL) and field-like (FL) spin-orbit effective fields in Pt(8)|Co(0.55-1.4)|Al(1.4)|Pt(3) sample. The top panel illustrates the DL geometry when $H \parallel I$ (H_x) and the FL geometry when $H \perp I$ (H_y) for a thin Co layer of magnetization M , at position (θ, ϕ) . a-b) In-plane field dependence of V_{2f} (green) for $t_{\text{Co}} = 0.9$ nm in (a) DL geometry and in (b) FL geometry. The solid black lines are fits to extract DLT and FLT. The horizontal axis is normalized with respect to the anisotropy field, H_K . The inset of Fig. 1a shows normalized V_f (green) as a function of in-plane magnetic field and Stoner-Wohlfarth fit (solid black lines). The data are shown after correcting the contributions from inhomogeneous device geometry as well as the thermal contributions as explained in Fig S2 and S3. (c) DL and (d) FL SOT fields *vs.* I for $t_{\text{Co}} = 0.55$ nm (disc), 0.9 nm (square) and 1.4 nm (star). The dotted lines are the linear fit forced to cross through (0,0) with uncertainty shown in shadow.

$$V_{2f}^{DL} = -1/2 \sin(\theta) \left(\frac{H_{DL} R_{AHE}}{H_K \cos(2\theta) - H \sin(\delta\theta_H - \theta)} + \frac{2H_{FL} R_{PHE} \sec(\delta\theta_H) \sin(\theta)}{H} \right) I_0. \quad (5)$$

In the similar way, for field-like (FL) geometry ($H \perp I$), $\theta_H = \pi/2 + \delta\theta_H$, $\phi = \phi_H = \pi/2$, and V_{2f} becomes:

$$V_{2f}^{FL} = 1/2 \cos(\theta) \sin(\theta) \left(\frac{H_{FL} R_{AHE}}{H_K \cos(2\theta) - H \sin(\delta\theta_H - \theta)} + \frac{2R_{PHE} H_{DL} \sec(\delta\theta_H) \sin(\theta)}{H} \right) I_0. \quad (6)$$

H_{DL} and H_{FL} are the damping-like and field-like effective fields, respectively. The values of R_{AHE} , H_K , $\theta(H)$ and $\delta\theta_H$ are extracted from V_f . We use the following procedure to extract the H_{FL} and H_{DL} :

- the first harmonic data is centered around zero.
- the amplitude of R_{AHE} is obtained from V_f vs $H_{x(y)}$ curve. In our case, the resistance $R_{AHE} = V_f/I$ at $H_{x(y)} = 0$. Additionally, R_{AHE} can also be obtained from DC measurements (see section IV).
- the V_f vs. $H_{x(y)}$ plot is normalized between +1 and -1 *i.e.* $\frac{V_f}{V_f(H_{x(y)}=0)}$ (inset of Fig. S1a).
- the normalized V_f vs. $H_{x(y)}$ curve is fitted by using the Stoner-Wohlfarth model (inset of Fig. 1a in the main text) allowing to extract the anisotropy field (H_K) and magnetic-field tilt ($\delta\theta_H$). We also interpolate the fit to obtain the magnetization rotation (θ) for each magnetic field.
- the base-line and thermal effects (if any) is removed from V_{2f} data. The procedure is explained in the section II.
- keeping H_{DL} and $H_{FL} \times R_{PHE}$ as a free parameter, V_{2f}^{DL} vs H_x is fitted to obtain H_{DL} and the $H_{FL} \times R_{PHE}$ product (see Fig. 1a in the main text).
- similarly keeping H_{FL} and the $H_{DL} \times R_{PHE}$ product as a free parameter, V_{2f}^{FL} vs. H_y is fitted to obtain H_{FL} and $H_{DL} \times R_{PHE}$ (see Fig. 1b in the main text).

The amplitude of V_{2f} predominantly depends on H_{DL} in the longitudinal geometry (V_{2f}^{DL}) and on H_{FL} in transverse geometry (V_{2f}^{FL}). In Fig. S1a-b, we show the dependence of second harmonic Hall voltage (V_{2f} , green points) acquired on a Pt(8)|Co(0.9)|Al(1.4)|Pt(3) sample as a function of in-plane magnetic fields in DL geometry and FL geometry. The inset of Fig. S1a shows the variation of first harmonic Hall voltage (V_f) vs. H_x fitted with Stoner-Wohlfarth model. The fit allows to extract the anisotropy fields (H_K) and the magnetization angle (θ) away from the easy-axis (z). Note that the accurate measurements of H_K and θ are critical prerequisites to extract precise values of H_{DL} and H_{FL} from V_{2f} . We also emphasize that extracting the effective fields by restricting to the linear regime of the V_{2f} may give rise to a strong discrepancy, especially in the estimation of H_{FL} values.

The H_{DL} and H_{FL} SOT components are determined by fitting V_{2f} vs. H_x and H_y respectively, and taking into account the contribution from the anomalous Hall (AHE) and planar Hall effects (PHE) [1]. We notice however that the PHE contribution is one order of magnitude smaller than the AHE and the fits are dominated by the first term of equation (5) and (6) in DL and FL geometries, respectively. The reported H_{DL} and H_{FL} values in the manuscript, are extracted from DL and FL geometries, respectively (by considering R_{PHE}). The fits are displayed by black continuous lines in Fig. S1a-b. In Fig. S1c-d, we show the H_{DL} and H_{FL} vs. $I = I_{RMS}$ for three Pt(8)|Co(t_{Co})|Al(1.4)|Pt(3) samples with Co thicknesses, $t_{Co} = 0.55, 0.9$ and 1.4 nm, which are in the range, or below the typical transverse spin decoherence length ($\lambda_{\perp} \approx 1.5 - 2$ nm) of Co [2, 3]. We note that H_{DL} changes sign with \mathbf{m} , whereas H_{FL} does not, in agreement with the expected SOT symmetries. The H_{DL} and H_{FL} are then measured at several currents and the slope of $H_{DL,FL}$ vs. I (dashed lines in Fig. S1(c-d)) is considered to compare the SOT fields between the samples for better accuracy. Furthermore, the SOT fields show linear scaling with current as expected. Additionally, the H_{FL} and Oersted field generated by current have the same symmetry. In our samples, we have estimated the Oersted field strength to be 0.7 G for 10^{11} A/m² current density in Pt, which, we have removed during the analysis.

II. CONTRIBUTION FROM THERMAL EFFECTS AND IMPERFECT DEVICE GEOMETRY IN FIRST AND SECOND HARMONIC HALL VOLTAGE

Asymmetric voltage contacts or defects in the device geometry as well as anomalous Nernst effect (ANE) might also contribute to the measured Hall voltage. Small misalignment in the voltage contacts leads to a constant offset (or a baseline) in V_f and V_{2f} and observed in almost all the devices. These effects (or the baseline) have been corrected in the raw data while analyzing the data. The raw measured V_f and the ones after correcting the offset as a function of the in-plane magnetic field are shown in Fig. S3a and Fig. S3d. The thermal effects mainly arise due to the ANE produced by an in-plane thermal gradient which generates an additional magnetization dependent voltage at the frequency $2f$. The amplitude of ANE voltage is determined by measuring the V_{2f} as a function of the out-of-plane magnetic field as shown in Fig. S2 (by keeping the magnetization out-of-plane $\theta = 0$). At $\theta = 0$, the SOT fields do not contribute to the V_{2f} (from equations 5 and 6, $V_{2f} = 0$ for $\theta = 0$) and the measured signal arises from spurious effects. The effect varies from sample to sample and the difference between V_{2f} at $+M_z$ and $-M_z$ is due to the ANE.

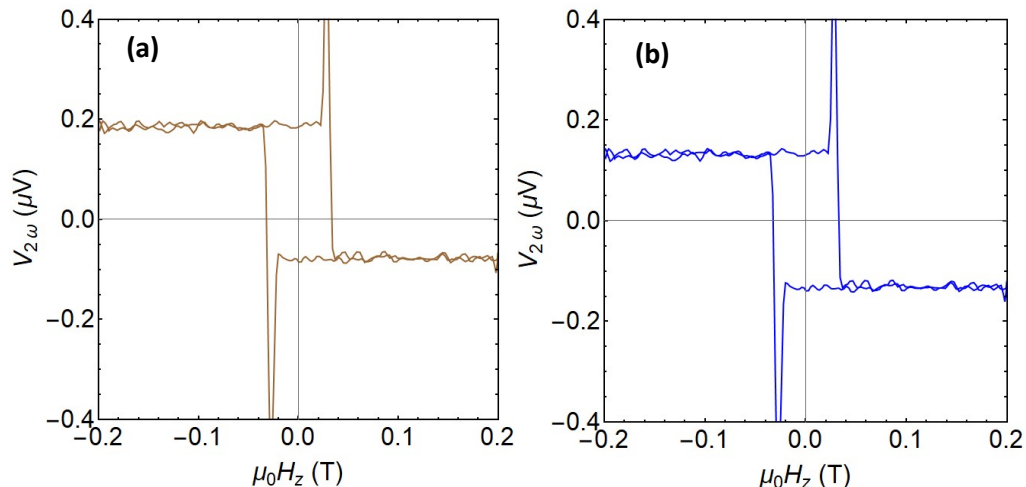


Figure S2. The anomalous Hall voltage at $2f$ as a function of out-of-plane magnetic field in Pt8|Co0.9|Cu1|Pt3 sample. (a) as measured (b) after an offset correction. The offset voltage arises due to misalignment at voltage contacts and the hysteresis kind of behaviour at $2f$ arises due to ANE.

We point out that the ANE voltage is always much smaller than the AHE voltage. The offset in data is due to the misalignment of voltage contacts as shown in Fig. S2a. The raw experimental data of V_{2f} as well as after subtracting an offset voltage and the ANE contribution are shown in Fig. S3 in both DL and FL geometries. We exclude these contributions during the fitting of our data to extract the SOT fields.

On the other hand, an out-of-plane thermal gradient may produce an additional V_{2f} contribution to the transverse signal only in the DLT measurement configuration when the magnetic field is sufficiently large to rotate the magnetization in the layer plane. Such "out-of-plane" ANE effects are expected to be maximum in the large field window over the in-plane saturation value that we did not observe for the whole sample series. Furthermore, in order to get rid of some possible thermal contributions, we have measured the contribution of out-of-plane thermal gradient into second harmonic Hall resistance by performing planar Hall effect measurements on thicker and in-plane magnetized "reference" Co samples. We have considered two different cases (i) a Pt/Co-based structure and (ii) in Co/oxide multilayer. In Fig. S3 (g), we show the amplitude of R_{2f} as a function of the external magnetic field in the two samples. The dotted lines are the fit involving possible thermal effects to separate the damping-like torque signal from the thermal effects. As the thermal effects are independent of the external magnetic field, the intercept of the linear fit is only due to the spurious contributions. As expected and observed, these effects contribute significantly to R_{2f} signal in the presence of an oxide interface, whereas the signal in Pt/Co sample is free from thermal contributions, which is presently our case.

III. VAN DER PAUW FOUR PROBE RESISTIVITY MEASUREMENTS AND CURRENT SHUNT IN PT.

The resistivity of each sample has been measured on thin films using van der Pauw method in four probe geometry. In Fig. S4, we show the sheet conductance, G_s ($=1/\text{sheet resistance}$, R_s) as a function of Pt thickness measured on $25 \mu\text{m}$ long and $5 \mu\text{m}$ wide devices in Ta(5)|Pt(t_{Pt})|Co(0.9)|Al(5) series of samples. The slope and intercept of the linear curve gives sheet conductance of 1 nm Pt and rest of the material in the stack (Ta(5)|Co(0.9)|Al(5)), respectively. From the slope, the resistivity of Pt $\rho_{\text{Pt}} = 24.2 \mu\Omega \times \text{cm}$ is determined. This method allows us to estimate also the interface resistance.

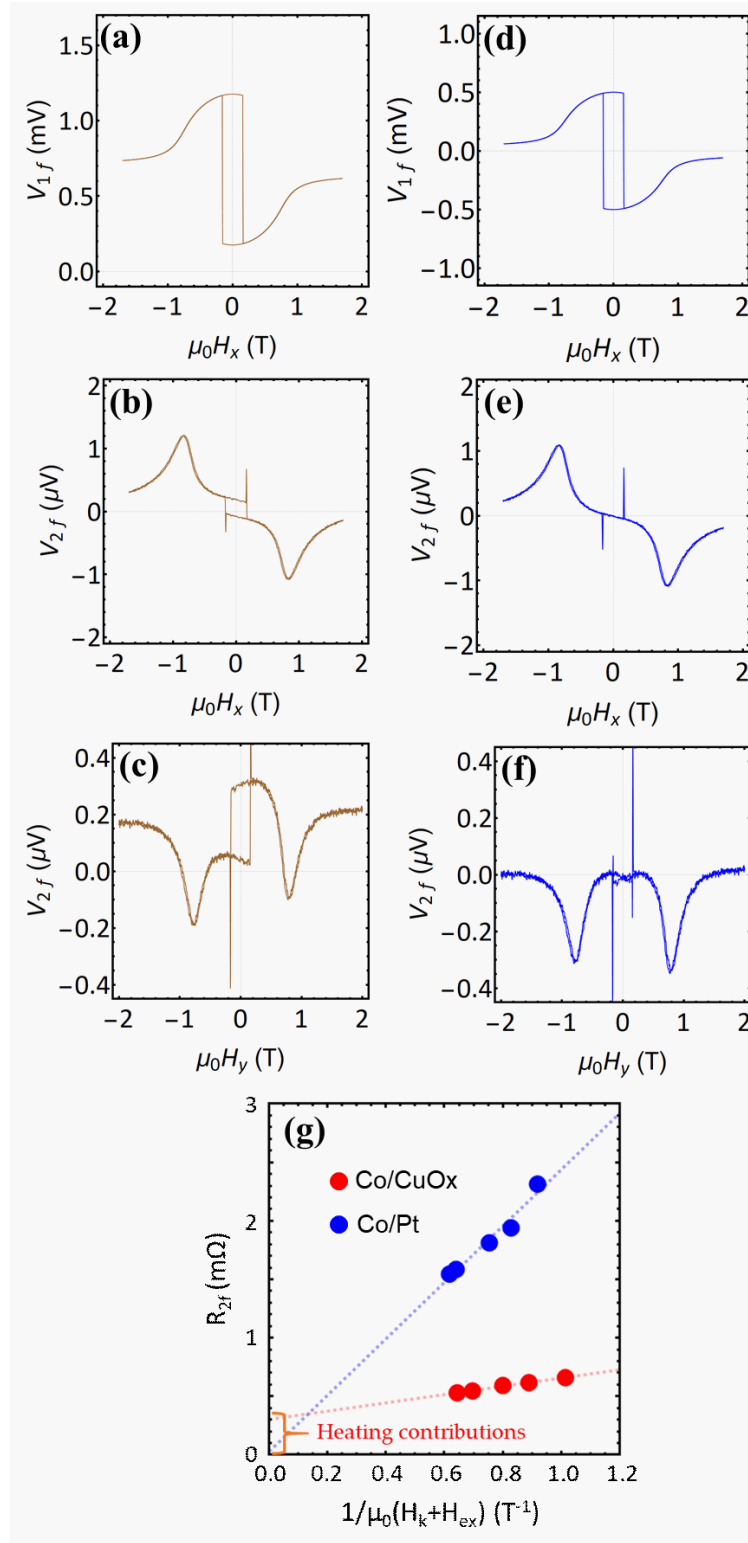


Figure S3. As measured (a) V_f voltage, (b) V_{2f} in DL geometry and (c) V_{2f} in FL geometry in Ta5|Pt8|Co0.9|Cu1|Pt3 sample. (d) The V_f after a continuous offset subtraction from the raw data. (e) The V_{2f} after a continuous offset and ANE correction in DL geometry. (f) The V_{2f} after a continuous offset and ANE correction in FL geometry. (g) Amplitude of R_{2f} as a function of external magnetic field (H_x) in two samples (i) Co/Pt samples in blue and (ii) Co/Oxide interface (red). The dotted lines are linear fits to separate the amplitude of SOTs from the thermal effects.

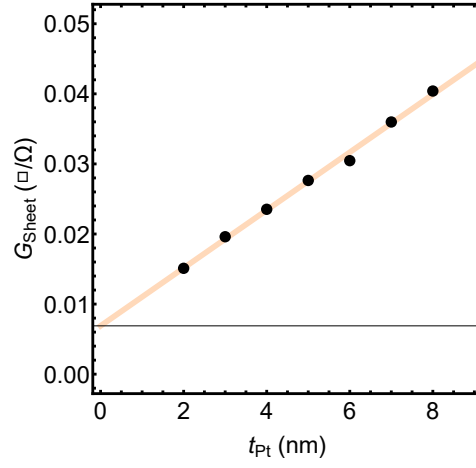


Figure S4. Sheet conductance of Ta(5)|Pt(t_{Pt})|Co(0.9)|Al(5) as a function of Pt thickness (black points), measured in four point van der Pauw geometry. The solid line is the linear fit to extract the resistivity of Pt.

The resistivities of Cu, Ta, Co and Al are also obtained from four-point geometries. To measure the shunt of the current density through Pt layer \mathcal{J}_{Pt} , we have used the following model:

$$\mathcal{J}_{Pt} = \frac{1}{\rho_{Pt}} \frac{t_{Pt} + t_{rest}}{\frac{t_{Pt}}{\rho_{Pt}} + \frac{t_{Rest}}{\rho_{Rest}}} \mathcal{J}_T \quad (7)$$

where \mathcal{J}_T is the total current density. In the similar way, the resistivity of Cu, Ta and Co was found to be $\sim 11.5\mu\Omega \times \text{cm}$, $\sim 169\mu\Omega \times \text{cm}$, and $\sim 30\mu\Omega \times \text{cm}$, respectively.

IV. ANOMALOUS HALL RESISTANCE, PLANAR HALL RESISTANCE, M_s AND ANISOTROPY FIELD.

A. Variation of M_s

We show below the values of the saturation magnetization measured on different sample series.

t_{Co}	M_s Pt8 Co(t_{Co}) Al1.4 Pt3 (MA/m)	M_s Pt8 Co(t_{Co}) Cu1.4 Pt3 (MA/m)
0.7 nm	1	1
0.9 nm	0.96	1.17
1.2 nm	1.13	1.23
1.4 nm	1.09	1.19

Table I. Values of the magnetization (MA/m) measured on the different series of samples.

B. Experimental AHE and PHE

In perpendicularly magnetized systems, the Hall resistance (R_H) is expressed as:

$$R_H = R_{AHE} \cos(\theta) + R_{PHE} \sin^2(\theta) \sin(2\phi), \quad (8)$$

where θ and ϕ are the polar and azimuthal angle of the magnetization (see Fig. S1), R_{AHE} is the anomalous Hall resistance and R_{PHE} is the planar Hall resistance. For each sample, we obtain the R_{AHE} by measuring the Hall resistance as a function of the out-of-plane magnetic field as shown in Fig. S5a. The R_{PHE} values are obtained by measuring the Hall voltage as a function of the in-plane angle between magnetization and current under a 3 T in-plane magnetic field. The 3 T magnetic field drags the magnetization in the plane *i.e.* $\theta = \pi/2$ and the variation in R_H solely arises due to the planar Hall effect. By replacing $\theta = \pi/2$ in Eq (7), we simply obtain:

$$R_H = R_{PHE} \sin(2\phi) \quad (9)$$

In Fig. S5b, we display the variation of R_H (black points) as a function of the in-plane field angle. We obtain R_{PHE} by fitting the data points with Eq (8). However, another way to obtain R_{PHE} is to measure the peak value as shown in Fig. S5b. The evolution of R_{AHE} in various series of sample is shown in Fig. S7. The anisotropy fields (H_K) of each sample is extracted by fitting first harmonic Hall voltage as a function of the in-plane magnetic field using Stonar-Wohlfarth model (inset of Fig. 1a of main text). The extracted anisotropy fields for Pt8|Co (t)|Al1.4|Pt3 and Pt8|Co (t)|Cu1.4|Pt3 series of samples are shown in Fig. S6.

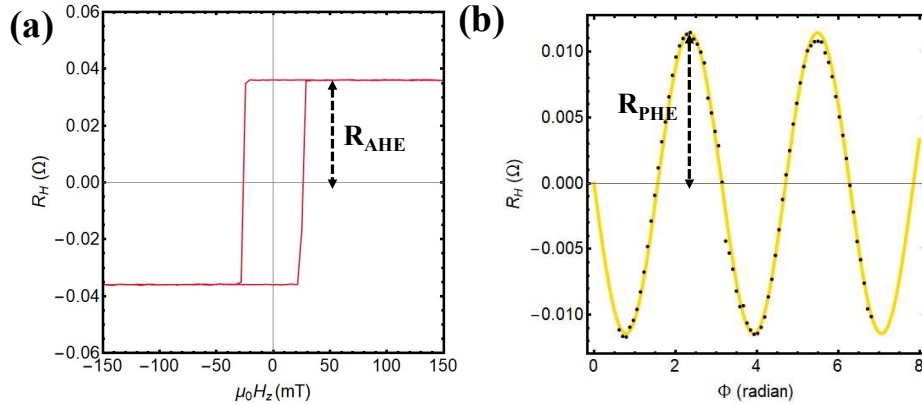


Figure S5. The Hall resistance (R_H) as a function of out-of-plane magnetic field in Pt8|Co0.7|Al1.4|Pt3 sample. The saturation value of R_H is the amplitude of R_{AHE} . (b) R_H (black points) as a function of angle (ϕ) between current ($100 \mu A$) and in-plane magnetization in the same sample. The solid yellow line is the fit to extract the R_{PHE} .

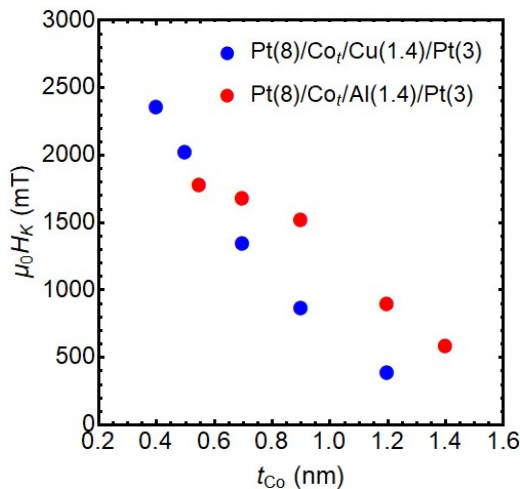


Figure S6. Anisotropy field in Pt8|Co(t_{Co})|Al1.4|Pt3 (red) and Pt8|Co(t_{Co})|Cu1.4|Pt3 (blue) as a function of Co thickness.

C. AHE analyses and spin-current proximity effects

Our analyses of Anomalous Hall effects (AHE) is based on a semi-phenomenological approach of spin-dependent transport, involving spin-dependent diffusion and electron scattering at the multiple interfaces, possibly considering spin-flips caused by the local spin-orbit interactions [4]. The principle of our analyses is then:

1) a representation of the spin-current profiles within the whole multilayers by correctly matching the out-of-equilibrium electronic Fermi distributions. This is of preliminary importance to provide the amplitude of the anomalous Hall effect (AHE) in multilayers as far as a ferromagnetic layer ensures the polarization of the current *via* the non-local spin-dependent conductivity calculated by our method.

2) Adjacent 5d SOC layers (*mainly Pt*) can affect the spin orbit assisted diffusion of electrons by *spin-current proximity effect*. Therefore, the AHE may be enhanced by increasing the spin orbit coupling in those SOC bottom and top Pt layers. The more important is the SOC, the largest is the transverse spin current *via* the spin-to-charge conversion process and the Anomalous Hall angle.

Apart from spin-dependent electronic diffusions in the bulk of the layers (*e.g* layer-dependent conductivity), one may emphasize the relevant boundary conditions to match for the out-of-equilibrium Fermi distribution in the framework of Fuchs-Sondheimer model. This is generally performed by including possible specular [4, 5] or diffusive reflection (\mathcal{R})/transmission(\mathcal{T}). Taking into account proximity (spin) currents effects we have calculated between layers (i) and layer ($i \pm 1$), the overall square resistance R_{xx} and transverse Hall resistance R_{xy} write respectively:

$$R_{xx} = \rho_{xx}^* \frac{L}{Wt} \simeq \frac{L}{W} \frac{1}{t \sigma_{xx}^*} = \frac{L}{W} \frac{1}{\sum_{i,\sigma} \sigma_{xx,i\sigma} t_i}, \quad (10)$$

$$R_{xy} \simeq \frac{\rho_{xy}^*}{t} = \frac{\sigma_{xy}^*}{t (\sigma_{xx}^*)^2} = \frac{\sum_{i,\sigma} (\sigma_{xy,i\sigma} t_i)}{\left(\sum_{i,\sigma} \sigma_{xx,i\sigma} t_i \right)^2} \quad (11)$$

where L , W represents the length and width of the Hall cross bars, t is the overall thickness of MLs and $\sigma_{xx,i\sigma}$ the local longitudinal spin-dependent conductivity of the i^{th} layer of thickness t_i and $\sigma_{xy,i\sigma}$ the local off-diagonal spin-conductivity in the layer (i).

We have gathered the physical parameters used for the AHE fitting in Table II. The transmission coefficients extracted and spin-memory loss are used to analyze the DLT and FLT torques in the main text.

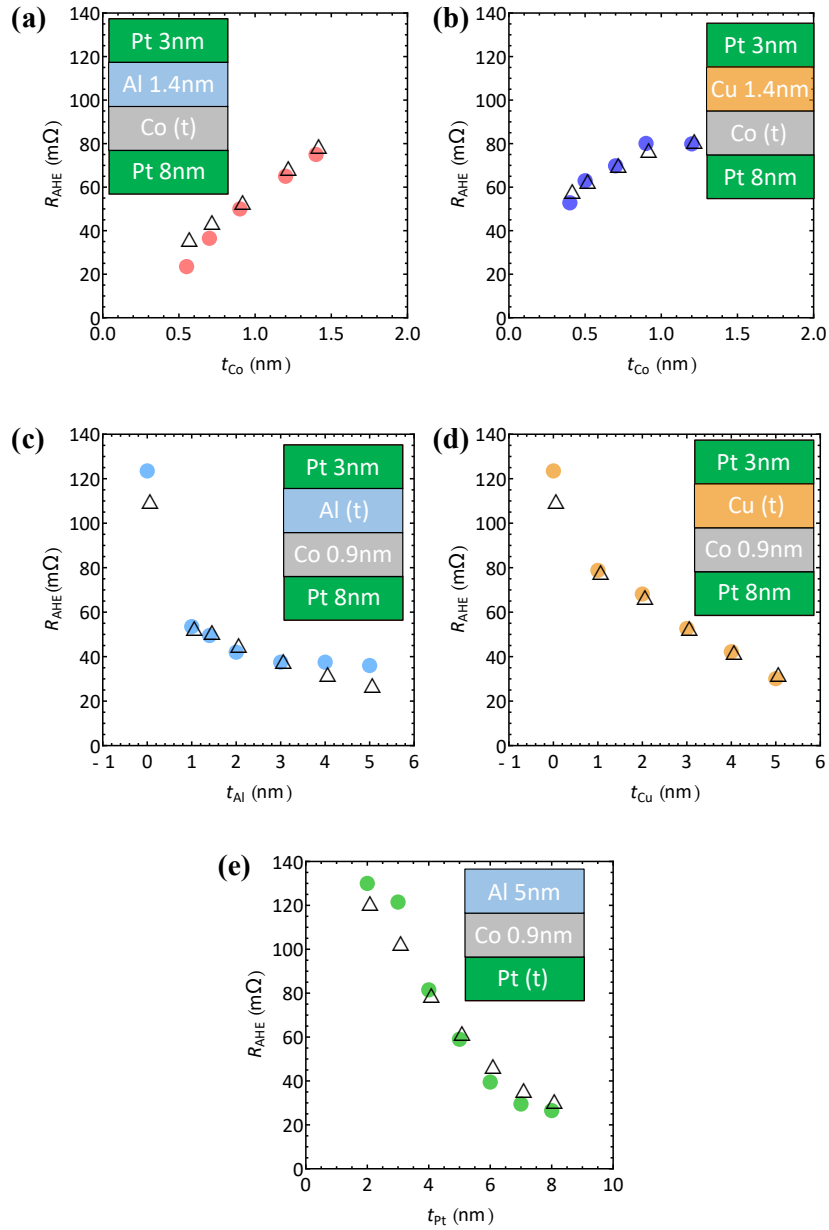


Figure S7. Anomalous Hall resistance (solid circles) in various series of samples. (a) In Pt8|Co(t_{Co})|Al1.4|Pt3 as a function of Co thickness. (b) In Pt8|Co(t_{Co})|Cu1.4|Pt3 as a function of Co thickness. (c) In Pt8|Co0.9|Al(t_{Al})|Pt3 as a function of Al thickness. (d) In Pt8|Co0.9|Cu(t_{Cu})|Pt3 as a function of Cu thickness. (e) In Pt(t_{Pt})|Co0.9|Al5 as a function of Pt thickness. The open triangles are the values of calculated R_{AHE} by considering current shunt (measured experimentally by using Van der Pauw method) in each layer. The multilayer stacking is shown in the inset of each plot.

Parameters	Symbols	Values for \uparrow spin	Value for \downarrow spin
Conductivity of Co	$\sigma_{Co} (S.cm^{-1})$	$\frac{\sigma_{Co}}{2(1-\beta_{Co})} = 7.4 \pm 1.0 \times 10^6$	$\frac{\sigma_{Co}}{2(1+\beta_{Co})} = 1.6 \pm 0.3 \times 10^6$
Conductivity of Cu	$\sigma_{Cu} (S.cm^{-1})$	$1.3 \pm 0.3 \times 10^7$	1.3 ± 0.310^7
Conductivity of Pt	$\sigma_{Pt} (S.cm^{-1})$	$2.5 \pm 0.5 \times 10^6$	$2.5 \pm 0.5 \times 10^6$
Conductivity of Al ₁₃₀	$\sigma_{Al} (S.cm^{-1})$	$7 \pm 1 \times 10^6$	$7 \pm 1 \times 10^6$
Mean free path of Co	$\lambda_{Co}(nm)$	7.0 ± 1	2.0 ± 0.3
Mean free path of Cu	$\lambda_{Cu}(nm)$	7.0 ± 1	7.0 ± 1
Mean free path of Pt	$\lambda_{Pt}(nm)$	2.0 ± 0.5	2.0 ± 0.5
Mean free path of Al	$\lambda_{Al}(nm)$	6.0 ± 1.5	6.0 ± 1.5
Bulk asymmetry coefficient of Co	β_{Co}	0.6 ± 0.1	
Spin Hall angle of Co	θ_{Co}	0.025 ± 0.01	-0.025 ± 0.01
Spin Hall angle of Pt	θ_{Pt}	0.22 ± 0.03	-0.22 ± 0.03
Spin Hall angle of Al	θ_{Al}	0.02 ± 0.01	-0.02 ± 0.01
Pt/Co Interface transmission	$\mathcal{T}_{Pt/Co}$	$\frac{\mathcal{T}_{Pt/Co}}{1-\gamma_{Pt/Co}} = 0.9 \pm 0.1$	$\frac{\mathcal{T}_{Pt/Co}}{1+\gamma_{Pt/Co}} = 0.4 \pm 0.1$
Co/Cu Interface transmission	$\mathcal{T}_{Co/Cu}$	$\frac{\mathcal{T}_{Co/Cu}}{1-\gamma_{Co/Cu}} = 0.9 \pm 0.05$	$\frac{\mathcal{T}_{Co/Cu}}{1+\gamma_{Co/Cu}} = 0.3 \pm 0.1$
Co/Al Interface transmission	$\mathcal{T}_{Co/Al}$	$\frac{\mathcal{T}_{Co/Al}}{1-\gamma_{Co/Al}} = 0.1 \pm 0.05$	$\frac{\mathcal{T}_{Co/Al}}{1+\gamma_{Co/Al}} = 0.1 \pm 0.05$
Cu/Pt Interface transmission	$\mathcal{T}_{Cu/Pt}$	$\mathcal{T}_{Cu/Pt} = 0.6 \pm 0.1$	$\mathcal{T}_{Cu/Pt} = 0.6 \pm 0.1$
Al/Pt Interface transmission	$\mathcal{T}_{Al/Pt}$	$\mathcal{T}_{Al/Pt} = 0.2 \pm 0.1$	$\mathcal{T}_{Al/Pt} = 0.2 \pm 0.1$
Pt/Co Interface asymmetry coefficient	$\gamma_{Pt/Co}$	0.5 ± 0.1	
Co/Cu Interface asymmetry coefficient	$\gamma_{Co/Cu}$	0.6 ± 0.1	
Co/Al Interface asymmetry coefficient	$\gamma_{Co/Al}$	0	
Pt/Co specularity in reflection	$sp_{Pt/Co}$	0.2 ± 0.1	
Co/Cu specularity in reflection	$sp_{Co/Cu}$	0.3 ± 0.1	
Co/Al specularity in reflection	$sp_{Co/Al}$	0.15 ± 0.1	
Cu/Pt specularity in reflection	$sp_{Cu/Pt}$	0.4 ± 0.1	
Al/Pt specularity in reflection	$sp_{Al/Pt}$	0	
Pt/Co spin-loss memory	$\delta_{Pt/Co}$	0.6 ± 0.1	
Co/Cu spin-loss memory	$\delta_{Co/Cu}$	0.3 ± 0.1	
Cu/Pt spin-loss memory	$\delta_{Cu/Pt}$	0.5 ± 0.1	
Co/Al spin-loss memory	$\delta_{Co/Al}$		

Table II. Physical parameters of Pt, Co, Cu and Al and their interfaces extracted from our AHE fitting procedure. Those values are compatible with the values extracted from the FLT and DLT torque fitting procedure. When not explicitly given, the error bars correspond to the value of the latest significant figure. The issue of specularity in reflection are largely discussed in Refs. [4, 5].

V. SIGN AND AMPLITUDE OF SOTS IN REFERENCE PT|CO|PT STACKS.

The amplitude and sign of current-induced effective fields are compared in Pt(8)|Co(0.9)|Pt(3), Pt(8)|Co(0.9)|Pt(8) and Pt(3)|Co(0.9)|Pt(8) samples by measuring second harmonic Hall voltage loops for reference. In Fig. S8, we show V_{2f}^{DL} loops, measured in DL geometry with the magnetic field applied along the current direction for the three samples. We observe sizable SOT effective field in Pt(8)|Co(0.9)|Pt(3) even though the structure is symmetric in terms of interfaces.

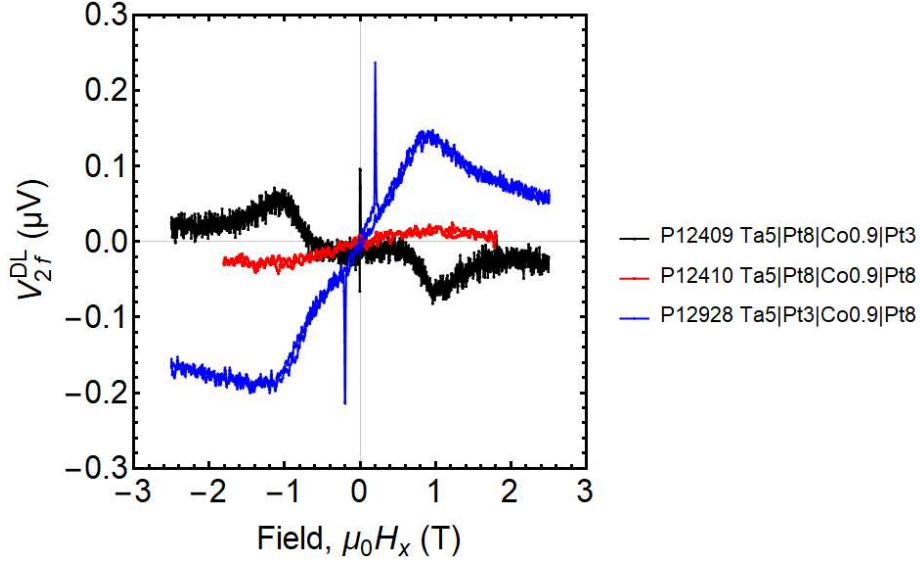


Figure S8. V_{2f}^{DL} as a function of in-plane magnetic field in DL geometry in Pt(8)|Co(0.9)|Pt(3) in black, Pt(8)|Co(0.9)|Pt(8) in red and Pt(3)|Co(0.9)|Pt(8) in blue.

This result suggests that spin current entering into Co from top 3 nm Pt is not large enough to compensate the effect of spin injection from bottom interface, in agreement with the results shown in Fig. 4a of the main text, for which at least 5 nm Pt is required to maximize the effect. To verify, we have measured torques in Pt(8)|Co(0.9)|Pt(8) sample, and as expected, we do not observe any SOT effective fields as shown by red curve in Fig. S8. The V_{2f}^{DL} curve in Pt(3)|Co(0.9)|Pt(8) sample (blue curve) has opposite polarity if compared to Pt(3)|Co(0.9)|Pt(8) (in black), which indicates the sign of SOT fields in Pt(3)|Co(0.9)|Pt(8) is opposite to that of Pt(8)|Co(0.9)|Pt(3) as expected.

VI. PT LAYER THICKNESS DEPENDENT EVOLUTION OF DL AND FL SOTS.

In Fig. 4b of the main text, we show the ratio of FL effective fields over DL effective fields as a function of Pt thickness in Pt(t_{Pt})|Co(0.9)|Al(8) stacks. The individual change in H_{FL} and H_{DL} as a function of Pt thickness is shown in Fig. S9. We note that when Pt thickness is smaller than 5 nm, both SOTs effective fields are decreasing with decreasing the Pt thickness. However it is important to mention that the rate of the change is different and we observe an increase in the ratio below 5 nm Pt (see Fig. 4b of the main text).

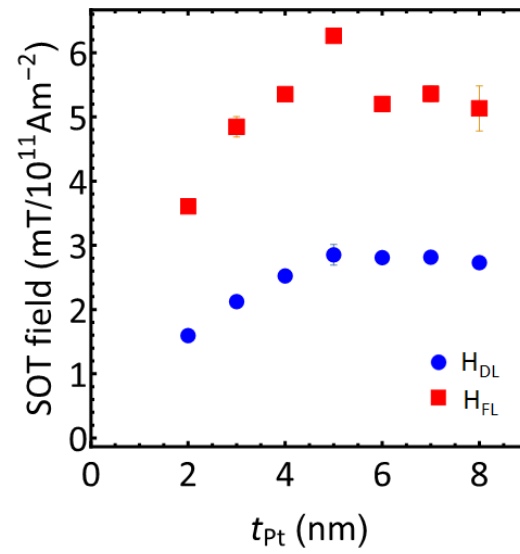


Figure S9. Damping-like and field-like effective fields as a function of Pt thickness for $10^{11} A/m^{-2}$ current density in Pt in $Pt(t_{Pt})|Co(0.9)|Al(5)$ stacks.

VII. MODELLING OF TORQUES IN MULTILAYERS.

SO torque related to SHE occur from the $4d$ or $5d$ host metallic materials [6], and is often described by a flow of spins transverse to the current satisfying the quantum law $\mathcal{J}_\sigma \propto \theta_{\text{SHE}} \mathcal{J}_c \times \hat{\sigma}$ [7–9] with θ_{SHE} , the spin-Hall angle (SHA) as the scaling parameter. It results in a linear relationship between the SHE-SOT and the applied electric field \mathcal{E} as $\tau_{\text{SOT}} \propto \sigma_{\text{SHE}}^{\text{eff}} \mathcal{E}$ with $\sigma_{\text{SHE}}^{\text{eff}}$ the spin Hall conductivity (SHE). Concerning the SOT related to REE, it arises that the charge current injected in the plane of an inversion asymmetric stack may produce a non-equilibrium spin-accumulation owing to a Rashba spin-structure, generally accompanying the spin-momentum locking (SML) [10]. The corresponding linear relationship is given by $\hat{\mu} \propto \kappa_{\text{IEE}} \mathcal{E}$, where $\kappa_{\text{IEE}} = \mathcal{N}^{\text{DOS}} \lambda_{\text{IEE}}$ is the Rashba-Edelstein tensor, λ_{IEE} the Rashba-Edelstein length and \mathcal{N}^{DOS} the 2-dimensional density of states (DOS). Importantly, this makes the REE distinct in nature from SHE. It is to be noticed that the spin-current and spin-accumulation generated by either origin, may act in concert to exert net SOT onto a magnetization vector $\hat{\mathbf{m}}$ with two different components: the damping-like torque (DLT) component, $\tau_{\text{DL}} \propto \hat{\mathbf{m}} \times (\hat{\mu} \times \hat{\mathbf{m}})$ and the field-like torque (FLT) component, $\tau_{\text{FL}} \propto \hat{\mu} \times \hat{\mathbf{m}}$ giving rise correspondingly to a damping-like (H_{DL}) and field-like (H_{FL}) effective fields.

A. Hypothesis and general framework: the generalized Boltzmann equation.

1. Coupled equations for spin-current and spin-accumulation (local spin-density).

To understand the experimental observations, we have modelled our results, and notably the different thickness dependence of the SOTs. Our modelling is adapted from the generalized drift-precession-diffusion equations and framework like proposed in Refs. [11–13]. These are shown to be in-line with the spin-dependent Boltzmann treatment [14]. We provide here subsequent numerical insights for H_{DL} and H_{FL} in strong agreement with the experimental data. We consider that the spin-orbit coupling in the $3d$ ferromagnetic transition metal (Co) is small enough and therefore, we add a small correction to the spin relaxation by taking into account the longitudinal (τ_{sf}) and transverse or decoherence (τ_Δ) spin-flip relaxation times. Consequently, the steady-state dynamics of both spin-accumulation and spin currents write:

$$\begin{aligned} \frac{\partial \hat{\mu}}{\partial t} &= -\frac{\hat{\mu}}{\tau_\Delta} - \frac{\hat{\mu}}{\tau_{sf}} - \frac{\hat{\mu} \times \hat{\mathcal{M}}}{\tau_J} - \frac{\partial \mathcal{J}_\sigma}{\partial z} \\ \frac{\partial \hat{\mathcal{J}}_\sigma}{\partial t} &= -\frac{\hat{\mathcal{J}}_\sigma}{\tau_\Delta} - \frac{\hat{\mathcal{J}}_\sigma}{\tau_p} - \frac{\hat{\mathcal{J}}_\sigma \times \hat{\mathcal{M}}}{\tau_J} - \frac{\mathcal{D}}{\tau_p} \frac{\partial \hat{\mu}}{\partial z} \end{aligned} \quad (12)$$

where $\hat{\mu}(z) = \text{Tr} \{ \langle \Psi_{kn} | \hat{\sigma} | \Psi_{kn} \rangle \}$ is the out-of equilibrium spin-density and $\mathcal{J}_\sigma(z)$ is the out-of equilibrium spin-current generated by SHE or REE. τ_J is the spin precessing time in Co, τ_Δ an extra transverse decoherence time (*i.e.* interactions with magnons), τ_p the momentum relaxation time ($\lambda = v_F \tau_p$ is the mean free path; v_F is the Fermi velocity), τ_{sf} is the longitudinal spin relaxation time and \mathcal{D} is the diffusion constant.

In the steady state regime of spin injection and spin-orbit torque ($\frac{\partial}{\partial t} = 0$), we obtain $\tilde{\mu} = \pm \frac{\tilde{\lambda}_\mu}{\tilde{\lambda}_p} \mathcal{J}_\sigma$ and $\mathcal{J}_\sigma = \pm \frac{\tilde{\lambda}_p}{\tilde{\lambda}_\mu} \tilde{\mu}$ for \mathcal{J}_σ and $\tilde{\mu} = \mu v_F$ (the local spin-density in the unit of a current) with $\tilde{\lambda}_p$ the characteristic (scaling) length of the spin eigenmode we are searching for. We have defined two intermediate complex dephasing lengths, either $\tilde{\lambda}_\mu = v_F (1/\tau_\Delta + 1/\tau_{sf} - i/\tau_J)^{-1}$ and $\tilde{\lambda}_J = v_F (1/\tau_\Delta + 1/\tau_p - i/\tau_J)^{-1}$. Hence, we find $\tilde{\lambda}_p = \sqrt{\tilde{\lambda}_J \tilde{\lambda}_\mu}$, the unique scaling length, characterized by a respective real (oscillatory part) and imaginary part $\lambda_\perp = \Im(\tilde{\lambda}_p)$, the transverse spin damping length previously defined.

We may also define a generalized spin-resistance for Co as $r_F^S = \frac{1}{G_{sh}} \sqrt{\frac{\tilde{\lambda}_\mu}{\tilde{\lambda}_J}}$ (G_{sh} is the Sharvin conductance), able to treat the spin-injection problem in a non-collinear magnetic configuration.

In the case of non-magnetic materials, it means that, without the exchange terms as for (Pt, Al, Cu), the product of the Sharvin conductance G_{sh} by the spin-resistance r^s , largely employed throughout the calculations, equals $\tilde{r}^s = G_{sh} r^s \approx \sqrt{\frac{\tau_{sf}}{\tau_p}}$ that is always larger than unity when the spin-lifetime τ_{sf} in the considered material is larger than the momentum relaxation time τ_p . Typical $\tilde{r}^s = G_{sh} r^s \approx \sqrt{\frac{\tau_{sf}}{\tau_p}}$ product values for Pt equals about $\tilde{r}^s \approx 2$ for $t_{\text{Pt}} = \infty$ whereas the corresponding value for 10 nm finite Cu and Al is larger than $\tilde{r}^s \gg 10$.

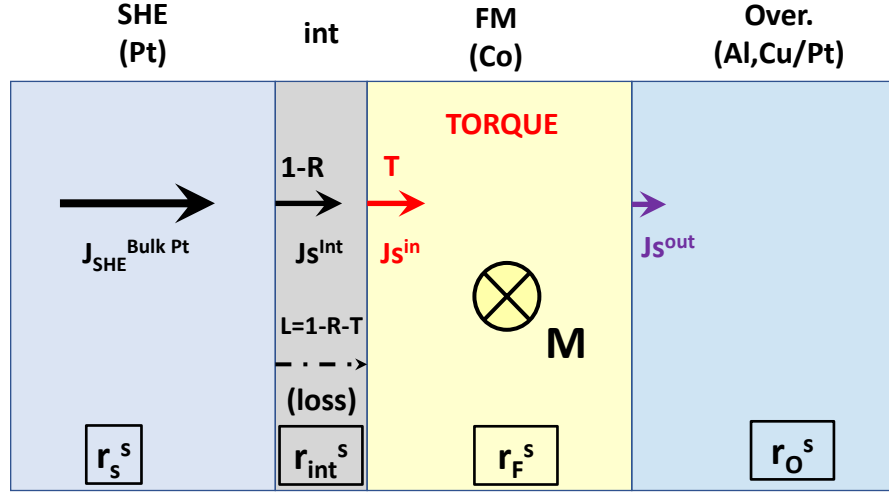


Figure S10. Sketch of the investigated multilayer structure constituted of a trilayer 'S/F/O' whereby a transverse spin-current is injected from a SHE 'S' material (Pt) into a thin ferromagnet 'F' (Co) and into an overlayer 'O'. Interfaces, e.g. Pt/Co, are treated as a thin dissipative interface layer (int) location of a spin-memory loss $\tilde{\mathcal{L}}$. The total amount of spin-current ejected from 'S' is noted $\mathcal{J}_s^{int} \propto 1 - \mathcal{R}$, whereas the proportion of the transverse spin-current injected in 'F' is noted $\mathcal{J}_s^{in} \propto \mathcal{T}$ and the one ejected from 'F' is \mathcal{J}_s^{out} . The integrated torque τ_{SOT} over the 'F' thickness is proportional to $\mathcal{J}_s^{in} - \mathcal{J}_s^{out}$. The different spin-resistance are noted $r_s^s, r_{int}^s, r_F^s, r_o^s$ respectively.

2. Torque calculations: analytical insights.

The integrated torque τ_{SOT} is calculated from the volume integral of the local torque due to the s - d exchange J_{xc} acting in parallel on the accumulation $\hat{\mu}_F$ in Co according to [15, 16]:

$$\tau_{SOT} = \int_{\mathcal{V}} \frac{d\hat{\mathcal{M}}}{d\tau} = - \int_{\mathcal{V}} \frac{\hat{\mathbf{m}} \times \hat{\mu}_F(z)}{\tau_J} d\mathcal{V} \quad (13)$$

where τ is the time, \mathcal{V} is the volume of Co, $\hat{\mathcal{M}}$ the magnetization of Co per unit volume, μ_F is expressed in the same unit (μ_B/\mathcal{V}) than $\hat{\mathcal{M}}$, and $\hat{\mathbf{m}}$ being the direction of the magnetization vector and $\tau_J = \frac{\hbar}{\mathcal{J}_{exc}}$ (\mathcal{J}_{exc} is the s - d exchange interaction).

In the presence of additional decoherence processes other than dephasing by precession and from Eq. [10], the knowledge of the transverse spin-current profile allows a rapid determination of the two SOT components.

From the generic equation [12]:

$$\frac{\hat{\mu}_F}{\tau_{\Delta}} + \frac{\hat{\mu}_F}{\tau_{sf}} + \frac{\hat{\mu}_F \times \hat{\mathcal{M}}}{\tau_J} = - \frac{\partial \mathcal{J}_{\sigma}}{\partial z} \quad (14)$$

we can extract:

$$\hat{\mu}_F = \frac{i\tau_J}{1 - i\tau_J \left(\frac{1}{\tau_{\Delta}} + \frac{1}{\tau_{sf}} \right)} \frac{\partial \mathcal{J}_{\sigma}}{\partial z} \quad (15)$$

together with the integrated torque τ_{SOT} according to:

$$\tau_{SOT} = - \frac{1 + i\tau_J \left(\frac{1}{\tau_{\Delta}} + \frac{1}{\tau_{sf}} \right)}{1 + \left[\tau_J \left(\frac{1}{\tau_{\Delta}} + \frac{1}{\tau_{sf}} \right) \right]^2} (\mathcal{J}_{\sigma}^{in} - \mathcal{J}_{\sigma}^{out}) \quad (16)$$

from Eq. [13], in which the $\mathcal{J}_\sigma^{in/out}$ are the respective *ingoing/outgoing* transverse spin-current from the Co ferromagnetic layer. Such generic expression for torques holds for REE too. In agreement with experimental data for Cu and Al samples, we then treat the REE as the effect of an additional spin accumulation $\hat{\mu}_{RE}$ in both sample series.

3. Boundary conditions for the spin-current/spin-density.

In this section we give more details about the calculation techniques. The spin information propagating in the multilayers is either given by the profile of the out-of equilibrium spin current $\mathcal{J}_\sigma(z)$ and/or spin-density $\hat{\mu}(z)$ along the thickness coordinate z . In each layer (l) (Pt, Co, Al, Cu) constituting the multilayers, the spin-current and spin accumulation can be represented as:

$$\mathcal{J}_\sigma(z) = \mathcal{J}_\sigma^{\Sigma(l)} + \Delta\mathcal{J}_\sigma^{(l)-} \exp\left(-\frac{z}{\tilde{\lambda}_p^{(l)}}\right) + \Delta\mathcal{J}_\sigma^{(l)+} \exp\left(+\frac{z}{\tilde{\lambda}_p^{(l)}}\right) \quad (17)$$

$$\mu_\sigma(z) = \mu_\sigma^{\Sigma(l)} + \Delta\mu_\sigma^{(l)-} \exp\left(-\frac{z}{\tilde{\lambda}_p^{(l)}}\right) + \Delta\mu_\sigma^{(l)+} \exp\left(+\frac{z}{\tilde{\lambda}_p^{(l)}}\right) \quad (18)$$

where $\mathcal{J}_\sigma^{\Sigma(l)}$ is the SHE current source and $\mu_\sigma^{\Sigma(l)}$ is the REE spin-density source in the layer (l). $\Delta\mathcal{J}_\sigma^{(l)\pm}$ and $\Delta\mu_\sigma^{(l)\pm}$ are the out-of-equilibrium quantities generated from interfaces by SHE and/or by REE. We are searching from our scattering matrix procedure. From the above dynamical equations, we then obtain a direct relationship linking $\Delta\mu_\sigma^{(l)\pm}$ and $\Delta\mathcal{J}_\sigma^{(l)\pm}$ according to $\frac{\Delta\mu_\sigma^{(l)\pm}}{\mathcal{N}^{DOS}\mu_B} = \mp er_F^S \Delta\mathcal{J}_\sigma^{(l)\pm}$ ($\mu_B = e\hbar/m$ is the Bohr magneton and \mathcal{N}^{DOS} is the 3D density of states (DOS)).

The general self-consistent solutions can then be solved by using either $\Delta\mathcal{J}_\sigma^{(l)\pm}$ or $\Delta\mu_\sigma^{(l)\pm}$ as unknown physical quantities. We chose the $\Delta\mathcal{J}_\sigma^{(l)\pm}$ basis able to treat both SHE and REE owing to the relevant boundary conditions to be used in each case (SHE or REE) separately.

Boundary conditions to be used to find the two *outward* out-of-equilibrium components $\Delta\mathcal{J}_\sigma^{(l)-}$ and $\Delta\mathcal{J}_\sigma^{(l+1)+}$ at a given interface $l/(l+1)$ between two consecutive layers (l) and ($l+1$) *vs.* *i*) the two *incoming* spin-current sources $\mathcal{J}_\sigma^{\Sigma(l)+}$ and $\mathcal{J}_\sigma^{\Sigma(l+1)-}$ as well as *ii*) the *inward* out-of-equilibrium spin-current components $\Delta\mathcal{J}_\sigma^{(l)+}$ and $\Delta\mathcal{J}_\sigma^{(l+1)-}$ are:

1 - the continuity of the total current when the spin-memory loss is zero according to:

$$\mathcal{J}_\sigma^{\Sigma(l)+} - \Delta\mathcal{J}_\sigma^{(l)-} + \Delta\mathcal{J}_\sigma^{(l)+} = -\mathcal{J}_\sigma^{\Sigma(l+1)+} + \Delta\mathcal{J}_\sigma^{(l+1)+} - \Delta\mathcal{J}_\sigma^{(l+1)-} \quad (19)$$

2 - equality between diffusive current and pure interface spin-current parametrized by the spin-mixing conductance with negligible spin-orbit $G_{\uparrow\downarrow}$ [17, 18] according to:

$$\mathcal{J}_\sigma^{\Sigma(l)+} - \Delta\mathcal{J}_\sigma^{(l)-} + \Delta\mathcal{J}_\sigma^{(l)+} = G_{\uparrow\downarrow} \left[r^{s(l)} \left(\Delta\mathcal{J}_\sigma^{(l)-} + \Delta\mathcal{J}_\sigma^{(l)+} \right) - r^{s(l+1)} \left(\Delta\mathcal{J}_\sigma^{(l+1)-} + \Delta\mathcal{J}_\sigma^{(l+1)+} \right) \right] \quad (20)$$

when the spin-memory is absent.

3 - incorporate the form of the spin-current discontinuity at the same interface if the spin-memory loss is present as well as an interface resistance r_b considering that the corresponding interfacial spin-resistance is $r_{int}^s = \frac{r_b}{\delta} = \frac{1}{G_s \delta}$ with G_s being the surface conductance. This overall calculation is performed by implementing the effective spin-transmission/reflection with loss. In the case of spin memory loss, the connection between the spin-mixing conductance $G_{\uparrow\downarrow}$ and the surface conductance G_s writes $G_{\uparrow\downarrow}^{-1} = G_s^{-1} + (r_F^s)^{-1}$ (see following paragraph).

B. The contribution from the spin-Hall effect.

1. Semi-phenomenological description: extended Boltzmann equation in the spin injection/diffusion/precession regime.

We first consider the solution of the generalized Boltzmann equation describing the profile of the spin-current and local spin-density (spin-accumulation) in the framework of the 'spin-injection' problem. This includes the formalism of complex spin-resistance of the ferromagnet r_s^F and interfacial G_s and/or spin-mixing conductance $G_{\uparrow\downarrow}$.

The trilayer structure of the type 'S/F/O' (Fig. S10) is constituted by two semi-infinite materials 'S' and 'O', where 'S' is typically played by the SHE material (*e. g.* Pt) and 'O' by the top part of the structure (*overlayer*). 'F' is the ferromagnetic material of thickness t_{Co} . We note $\tilde{t}_S = \frac{t_s}{\lambda_s}$ and $\tilde{t}_F = \frac{t_{Co}}{\lambda_p}$ the reduced thicknesses of 'S' and 'F' respectively (over their spin-relaxation length). We consider G_s the generalized surface spin conductance of the S/F interface depending on the surface transparency (the so-called spin-mixing conductance $G_{\uparrow\downarrow}$ will be defined afterwards Vs. G_s) and r_{int}^s , r_F^s and r_O^s the spin-resistance of the different materials (*int* for the interface, r_F is the generalized spin-resistance of the thin ferromagnet). From the diffusive theory of spin injection, one can extract the profile of the SHE spin-current in the depth of the structure and give in particular the expression of the respective ingoing ('*in*') and outgoing ('*out*') spin-current in/out the 'F' layer according to:

$$\begin{aligned} \frac{\mathcal{J}_{SHE}^{int}}{J_{SHE}^{bulkPt}} &= \frac{\tilde{r}_S^s (1 - \text{sech } \tilde{t}_s) [\tilde{r}_{int}^s \cosh \delta (\tilde{r}_F^s \cosh \tilde{t}_F + \tilde{r}_O^s \sinh \tilde{t}_F) + \tilde{r}_F^s \sinh \delta (\tilde{r}_F^s \sinh \tilde{t}_F + \tilde{r}_O^s \cosh \tilde{t}_F)]}{\tilde{r}_{int}^s (\tilde{r}_S^s \cosh \delta + \tilde{r}_{int}^s \sinh \delta) (\tilde{r}_F^s \cosh \tilde{t}_F + \tilde{r}_O^s \sinh \tilde{t}_F) + \tilde{r}_F^s (\tilde{r}_S^s \sinh \delta + \tilde{r}_{int}^s \cosh \delta) (\tilde{r}_F^s \sinh \tilde{t}_F + \tilde{r}_O^s \cosh \tilde{t}_F)} \\ \frac{\mathcal{J}_s^{in}}{J_{SHE}^{bulkPt}} &= \frac{\tilde{r}_S^s (1 - \text{sech } \tilde{t}_s) \tilde{r}_{int}^s (\tilde{r}_F^s \cosh \tilde{t}_F + \tilde{r}_O^s \sinh \tilde{t}_F)}{\tilde{r}_{int}^s (\tilde{r}_S^s \cosh \delta + \tilde{r}_{int}^s \sinh \delta) (\tilde{r}_F^s \cosh \tilde{t}_F + \tilde{r}_O^s \sinh \tilde{t}_F) + \tilde{r}_F^s (\tilde{r}_S^s \sinh \delta + \tilde{r}_{int}^s \cosh \delta) (\tilde{r}_F^s \sinh \tilde{t}_F + \tilde{r}_O^s \cosh \tilde{t}_F)} \\ \frac{\mathcal{J}_s^{out}}{J_{SHE}^{bulkPt}} &= \frac{\tilde{r}_S^s (1 - \text{sech } \tilde{t}_s) \tilde{r}_{int}^s \tilde{r}_F^s}{\tilde{r}_{int}^s (\tilde{r}_S^s \cosh \delta + \tilde{r}_{int}^s \sinh \delta) (\tilde{r}_F^s \cosh \tilde{t}_F + \tilde{r}_O^s \sinh \tilde{t}_F) + \tilde{r}_F^s (\tilde{r}_S^s \sinh \delta + \tilde{r}_{int}^s \cosh \delta) (\tilde{r}_F^s \sinh \tilde{t}_F + \tilde{r}_O^s \cosh \tilde{t}_F)} \end{aligned}$$

with J_{SHE}^{bulkPt} the bulk spin-Hall current and considering the finite transmission at the S/F interface ($\propto \frac{1}{r_{int}^s}$) and the spin-memory loss parametrized by the δ parameter. This yields:

$$\begin{aligned} \frac{\mathcal{J}_s^{in}}{J_{SHE}^{bulkPt}} &= \frac{\tilde{G}_s \tilde{r}_S^s (1 - \text{sech } \tilde{t}_s) (\tilde{r}_F^s \cosh \tilde{t}_F + \tilde{r}_O^s \sinh \tilde{t}_F)}{\left(\frac{\sinh \delta}{\delta} + \tilde{G}_s \tilde{r}_S^s \cosh \delta \right) (\tilde{r}_F^s \cosh \tilde{t}_F + \tilde{r}_O^s \sinh \tilde{t}_F) + \tilde{G}_s \tilde{r}_F^s (\cosh \delta + \tilde{G}_s \tilde{r}_S^s \delta \sinh \delta) (\tilde{r}_F^s \sinh \tilde{t}_F + \tilde{r}_O^s \cosh \tilde{t}_F)} \\ \frac{\mathcal{J}_s^{out}}{J_{SHE}^{bulkPt}} &= \frac{\tilde{G}_s \tilde{r}_S^s (1 - \text{sech } \tilde{t}_s) \tilde{r}_F^s}{\left(\frac{\sinh \delta}{\delta} + \tilde{G}_s \tilde{r}_S^s \cosh \delta \right) (\tilde{r}_F^s \cosh \tilde{t}_F + \tilde{r}_O^s \sinh \tilde{t}_F) + \tilde{G}_s \tilde{r}_F^s (\cosh \delta + \tilde{G}_s \tilde{r}_S^s \delta \sinh \delta) (\tilde{r}_F^s \sinh \tilde{t}_F + \tilde{r}_O^s \cosh \tilde{t}_F)} \end{aligned}$$

with \tilde{G}_s being the surface conductance in unit of G_{sh} . The integrated torque is given by Eq. [16] to give:

$$\frac{\tau_{SOT}}{J_{SHE}^{bulkPt}} \sim \frac{\tilde{G}_s \tilde{r}_S^s (1 - \text{sech } \tilde{t}_s) [\tilde{r}_F^s (\cosh \tilde{t}_F - 1) + \tilde{r}_O^s \sinh \tilde{t}_F]}{\left(\frac{\sinh \delta}{\delta} + \tilde{G}_s \tilde{r}_S^s \cosh \delta \right) (\tilde{r}_F^s \cosh \tilde{t}_F + \tilde{r}_O^s \sinh \tilde{t}_F) + \tilde{G}_s \tilde{r}_F^s (\cosh \delta + \tilde{G}_s \tilde{r}_S^s \delta \sinh \delta) (\tilde{r}_F^s \sinh \tilde{t}_F + \tilde{r}_O^s \cosh \tilde{t}_F)}$$

where we remind that $\tilde{t} = \frac{t}{\lambda_p}$.

In the limit of zero spin-memory loss $\delta = 0$, one gets:

$$\begin{aligned} \frac{\tau_{SOT}}{J_{SHE}^{bulkPt}} &\sim \frac{\tilde{G}_s \tilde{r}_S^s (1 - \text{sech } \tilde{t}_s) [\tilde{r}_F^s (\cosh \tilde{t}_F - 1) + \tilde{r}_O^s \sinh \tilde{t}_F]}{\left(1 + \tilde{G}_s \tilde{r}_S^s \right) (\tilde{r}_F^s \cosh \tilde{t}_F + \tilde{r}_O^s \sinh \tilde{t}_F) + \tilde{G}_s \tilde{r}_F^s (\tilde{r}_F^s \sinh \tilde{t}_F + \tilde{r}_O^s \cosh \tilde{t}_F)} \\ \frac{\tau_{SOT}}{J_{SHE}^{bulkPt}} &\sim \frac{\tilde{G}_{\uparrow\downarrow} \tilde{r}_S^s (1 - \text{sech } \tilde{t}_s) [\tilde{r}_F^s (\cosh \tilde{t}_F - 1) + \tilde{r}_O^s \sinh \tilde{t}_F]}{\left(1 + \tilde{G}_{\uparrow\downarrow} \tilde{r}_S^s \right) (\tilde{r}_F^s \cosh \tilde{t}_F + \tilde{r}_O^s \sinh \tilde{t}_F) + \tilde{G}_{\uparrow\downarrow} \tilde{r}_F^s (\tilde{r}_O^s - \tilde{r}_F^s) \exp(-\tilde{t}_F)} \end{aligned} \quad (21)$$

after having defined the spin-mixing conductance $G_{\uparrow\downarrow}$ as $G_{\uparrow\downarrow}^{-1} = G_s^{-1} + (r_F^s)^{-1}$.

In order to catch the underlying mechanism, two different cases have to be discussed:

(i) The infinite 'FM' thickness (thickness large compared to the decoherence length) giving:

$$\frac{\tau_{SOT}}{J_{SHE}^{bulkPt}} \sim \frac{\tilde{G}_{\uparrow\downarrow} \tilde{r}_S^s (1 - \text{sech } \tilde{t}_s)}{1 + \tilde{G}_{\uparrow\downarrow} \tilde{r}_S^s} \quad (22)$$

being essentially a real quantity (because $\tilde{G}_{\uparrow\downarrow}$ is mainly real) giving rise to an almost pure Damping-like torque (DLT) like already discussed [19] and formula we have used in the article text (Eq. [3]).

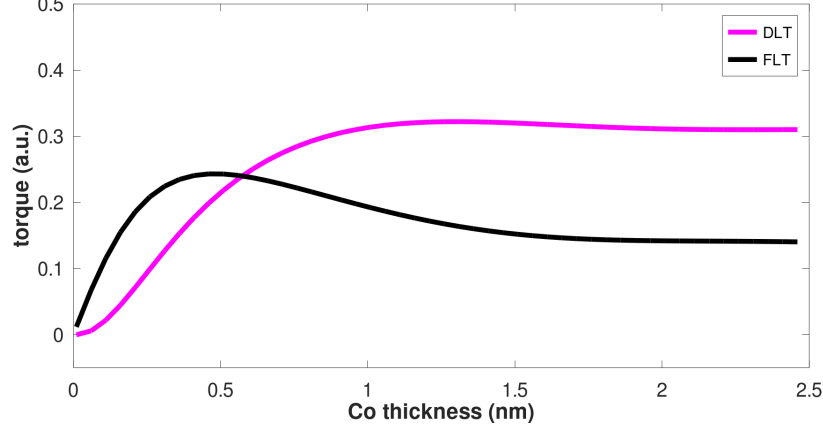


Figure S11. Ferromagnetic layer thickness (t_{Co}) dependence of the two torque components, *respectively* DLT and FLT, calculated on a Pt8|Co(t_{Co})|Al(1.4)|Pt(3). The limit at small t_{Co} displays a linear dependence of the FLT and a quadratic dependence of the DLT as expected from the theory.

(ii) The limit of zero 'FM' thickness (thickness small compared to the decoherence length) giving:

$$\frac{\tau_{SOT}}{\mathcal{J}_{SHE}^{bulk Pt}} \sim \left(\frac{\tilde{r}_O^s}{\tilde{r}_F^s} \right) \frac{\tilde{G}_{\uparrow\downarrow} \tilde{r}_S^s}{1 + \tilde{G}_{\uparrow\downarrow} \tilde{r}_S^s} (1 - \text{sech } \tilde{t}_s) \sinh \tilde{t}_F \quad (23)$$

Note that in the case of zero additional transverse decoherence $\tau_{\Delta} = \infty$, $\sinh \tilde{t}_F = i \frac{t_{Co}}{v_F \tau_J}$ is purely imaginary and, in that limit, the torque is mostly field-like (FLT) showing, as expected, a linear dependence on t_{Co} . This explains a part of our findings on Pt|Co|Cu|Pt systems. From these calculations, in the limit of zero 'F' film thickness, the DLT (real part of τ) admits a square dependence t_{Co}^2 on the thickness (see Fig. S11). Moreover, the involvement of additional decoherence processes $\tau_{\Delta} \lesssim \tau_J$ reinforces the strength of the FLT compared to DLT owing to the prefactor in Eq. [16] as discussed previously in the case of ferromagnetic semiconductors [20].

2. Numerical implementation in the multilayer scattering framework [4]

We now turn on the numerical implementation of the theory previously described which uses multiple interface scattering formalism (electronic reflection/transmission and subsequent interferences) where all the conductance quantities and inverse of spin-resistance are scaled down by the Sharvin conductance (G_{Sh}). In particular, such implementation also involves complex propagating functions in the Co ferromagnet as previously described. We give now some details.

The effective transmission/reflection coefficients :

Considering the presence of the spin-memory loss with parameter δ [21], the effective transmission \mathcal{T} , reflection \mathcal{R} and loss \mathcal{L} for a transverse spin-current \mathcal{J}_{σ} propagating from the left (l) into the interface (l)/($l+1$) writes respectively:

$$\begin{aligned} \mathcal{T} &= \frac{T_{\uparrow\downarrow} \tilde{r}^{s(l)} \left(\frac{\delta}{\sinh \delta} \right)}{1 + \delta \coth \delta T_{\uparrow\downarrow} (\tilde{r}^{s(l)} + \tilde{r}^{s(l+1)}) + \delta^2 T_{\uparrow\downarrow}^2 \tilde{r}^{s(l)} \tilde{r}^{s(l+1)}} \\ \mathcal{R} &= \frac{1 + \delta \coth \delta T_{\uparrow\downarrow} \tilde{r}^{s(l+1)}}{1 + \delta \coth \delta T_{\uparrow\downarrow} (\tilde{r}^{s(l)} + \tilde{r}^{s(l+1)}) + \delta^2 T_{\uparrow\downarrow}^2 \tilde{r}^{s(l)} \tilde{r}^{s(l+1)}} \\ \mathcal{L} &= \frac{\delta T_{\uparrow\downarrow} \tilde{r}^{s(l)} \left(\tanh \frac{\delta}{2} + \delta T_{\uparrow\downarrow} \tilde{r}^{s(l+1)} \right)}{1 + \delta \coth \delta T_{\uparrow\downarrow} (\tilde{r}^{s(l)} + \tilde{r}^{s(l+1)}) + \delta^2 T_{\uparrow\downarrow}^2 \tilde{r}^{s(l)} \tilde{r}^{s(l+1)}} \end{aligned} \quad (24)$$

satisfying $\mathcal{T} + \mathcal{R} + \mathcal{L} = 1$.

The relative spin memory loss defined as the relative spin-current lost over the total spin-current ejected writes then:

$$\tilde{\mathcal{L}} = \frac{\mathcal{L}}{1 - \mathcal{R}} = \frac{\tanh \frac{\delta}{2} + \delta T_{\uparrow\downarrow} \tilde{r}^{s(l+1)}}{\coth \delta + \delta T_{\uparrow\downarrow} \tilde{r}^{s(l+1)}} \quad (25)$$

which increases with δ and approaches unity when $\delta \rightarrow \infty$. Note that this expression of $\tilde{\mathcal{L}}$ does not depend of the spin-resistance $r^{s(l)}$ of the material from which the carriers are injected.

Other equivalent expression of Eqs.[24] exist for the effective transmission $\tilde{\mathcal{T}}$ and reflection coefficients $\tilde{\mathcal{R}}$ related to inward out-of-equilibrium spin-accumulation components, $\Delta \mathcal{J}_\sigma^{(l)+}$ and $\Delta \mathcal{J}_\sigma^{(l+1)-}$, playing the role of sources according to:

$$\begin{aligned} \tilde{\mathcal{T}} &= \frac{2T_{\uparrow\downarrow} \tilde{r}^{s(l)} \left(\frac{\delta}{\sinh \delta} \right)}{1 + \delta \coth \delta T_{\uparrow\downarrow} (\tilde{r}^{s(l)} + \tilde{r}^{s(l+1)}) + \delta^2 T_{\uparrow\downarrow}^2 \tilde{r}^{s(l)} \tilde{r}^{s(l+1)}} \\ \tilde{\mathcal{R}} &= \frac{1 + \delta \coth \delta T_{\uparrow\downarrow} (\tilde{r}^{s(l+1)} - \tilde{r}^{s(l)})}{1 + \delta \coth \delta T_{\uparrow\downarrow} (\tilde{r}^{s(l)} + \tilde{r}^{s(l+1)}) + \delta^2 T_{\uparrow\downarrow}^2 \tilde{r}^{s(l)} \tilde{r}^{s(l+1)}} \end{aligned} \quad (26)$$

Equivalent formula exist for reciprocal transmission ($\tilde{\mathcal{T}}'$) and reflection ($\tilde{\mathcal{R}}'$) coefficients for carriers moving in an opposite direction.

The use of the scattering matrix:

We consider the respective $\mathcal{S} = \begin{bmatrix} \mathcal{R} & \mathcal{T}' \\ \mathcal{T}' & \mathcal{R}' \end{bmatrix}$ and $\tilde{\mathcal{S}} = \begin{bmatrix} \tilde{\mathcal{R}} & \tilde{\mathcal{T}}' \\ \tilde{\mathcal{T}}' & \tilde{\mathcal{R}}' \end{bmatrix}$, the respective scattering matrices linking the outward out-of-equilibrium spin-current components to the incoming sources according to:

$$\begin{pmatrix} \Delta \mathcal{J}_\sigma^{(l)-} \\ \Delta \mathcal{J}_\sigma^{(l+1)+} \end{pmatrix} = \mathcal{S} \begin{pmatrix} \mathcal{J}_\sigma^{\Sigma(l)+} \\ \mathcal{J}_\sigma^{\Sigma(l+1)-} \end{pmatrix} + \tilde{\mathcal{S}} \begin{pmatrix} \Delta \mathcal{J}_\sigma^{(l)+} \\ \Delta \mathcal{J}_\sigma^{(l+1)-} \end{pmatrix} \quad (27)$$

In our approach, the spin-current source $\begin{pmatrix} \mathcal{J}_\sigma^{\Sigma(l)+} \\ \mathcal{J}_\sigma^{\Sigma(l+1)-} \end{pmatrix}$ is treated as an effective out-of-equilibrium source term $\tilde{\mathcal{S}}^{-1} \mathcal{S} \begin{pmatrix} \mathcal{J}_\sigma^{\Sigma(l)+} \\ \mathcal{J}_\sigma^{\Sigma(l+1)-} \end{pmatrix}$ according to:

$$\begin{pmatrix} \Delta \mathcal{J}_\sigma^{(l)-} \\ \Delta \mathcal{J}_\sigma^{(l+1)+} \end{pmatrix} = \tilde{\mathcal{S}} \left[\tilde{\mathcal{S}}^{-1} \mathcal{S} \begin{pmatrix} \mathcal{J}_\sigma^{\Sigma(l)+} \\ \mathcal{J}_\sigma^{\Sigma(l+1)-} \end{pmatrix} + \begin{pmatrix} \Delta \mathcal{J}_\sigma^{(l)+} \\ \Delta \mathcal{J}_\sigma^{(l+1)-} \end{pmatrix} \right] \quad (28)$$

which allows to treat both sources in a universal scattering approach. We then solve self consistently the ensemble of the above equations treating the boundary conditions at each interface of the multilayers by employing the *scattering path operator* technique in such diffusive problem as largely employed in the multiple interface quantum scattering problem [4]. For the present case, this framework is generalized to the case of non-collinear magnetization geometry [17] with the introduction on complex propagating electronic wavevectors q with $q^{-1} = \lambda_p = v_F (1/\tau_\Delta + 1/\tau_{sf} - i/\tau_J) (1/\tau_\Delta + 1/\tau_p - i/\tau_J)$ [12].

The generalized multilayer scattering problem is then solved through a matrix inversion treatment of the recursive formula for $\tilde{\mathcal{S}}$ [22, 23]:

$$\left(\tilde{\mathcal{S}} \right)_{nm} = (\tilde{s})_{nn} \delta_{nm} + \left(\tilde{\mathcal{S}} \right)_{nl} \mathcal{P}_{lm} (\tilde{s})_{mm} \quad (29)$$

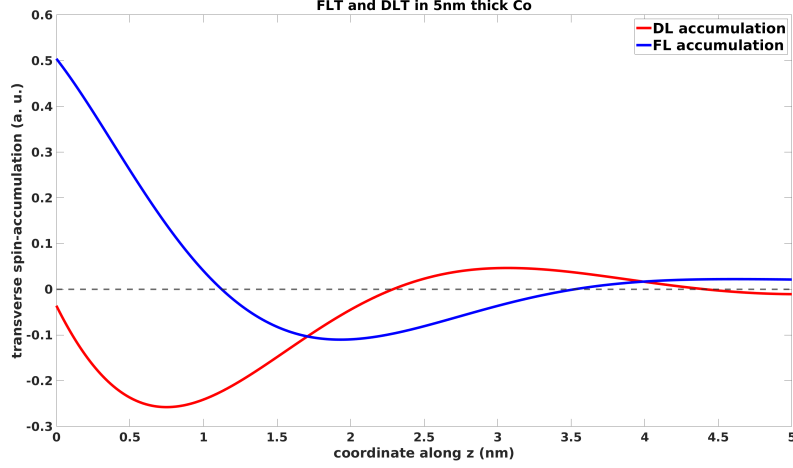


Figure S12. Spatial dependence of the out-of-equilibrium spin (spin-accumulation) and/or SOT components injected in a 5 nm Co layer. The blue curve correspond to transverse spin-accumulation parallel to the incoming SHE spin direction (responsible for FLT). The red curve is the component transverse to both the magnetization and SHE spin-current injected (responsible for DLT).

with $\tilde{s}_{nn} = \begin{bmatrix} \tilde{\mathcal{R}}_{nn} & \tilde{\mathcal{T}}'_{nn} \\ \tilde{\mathcal{T}}'_{nn} & \tilde{\mathcal{R}}'_{nn} \end{bmatrix}$ the *bare* scattering matrix at the single interface (n), \mathcal{P}_{lm} the propagation matrix in a given layer (l) from the interface (l) to the interface (m) ($m = m \pm 1$). $\tilde{\mathcal{S}}_{nl}$ is the *super scattering matrix* we are searching for corresponding to an *ingoing* spin-injection at the interface (n) and an *outgoing* scattering out-of the interface (m).

C. Parameters used and resulting modelling:

For the fit of Figs. [2,3,4] in the main text, we have extracted:

- precession length parameter: $\lambda_J = 2\pi v_F \tau_J = 4.7$ nm
- transverse spin decoherence length $\lambda_{\perp} = 1.7$ nm

with the use of the following parameters for Co|Pt and Co|Cu|Pt [4, 24, 25]:

- average spin mean free path in Co: $\lambda_{Co} = v_F \tau_p = 4$ nm
- reduced spin resistance for Pt : $\tilde{r}_{Pt}^s = G_{sh} \times r_{Pt}^s = 2$ with $G_{sh} \approx 4 \times 10^{15}$ S/m² (obtained from the value of $G_{\uparrow\downarrow}^{Co/Pt}$ [21]) and $r_{Pt}^s = \rho_{Pt} \times \lambda_{sf}^{Pt}$ ($\rho_{Pt} \approx 25 \mu\Omega \cdot \text{cm}$ and $\lambda_{sf}^{Pt} = 1.5$ nm).
- reduced spin resistance for Al(1.4)|Pt and Cu(1.4)|Pt : $\tilde{r}_{(Al,Cu)/Pt}^s = G_{sh} \times r_{(Al,Cu)/Pt}^s = 3$.
- spin-Hall angle of Pt (considering spin loss): $\theta_{SHE}^{bulkPt} = \frac{\mathcal{J}_{SHE}^{bulkPt}}{\mathcal{J}_c} = 0.22 \pm 0.03$ where \mathcal{J}_c is the charge current.
- spin-mixing transmission $\mathcal{T}_{\uparrow\downarrow}^{Co|Pt} = \frac{G_{\uparrow\downarrow}}{G_{sh}}$ at the Co|Pt interface $\mathcal{T}_{\uparrow\downarrow}^{Co|Pt} = 0.8$
- spin-mixing transmission $\mathcal{T}_{\uparrow\downarrow}^{Co|Cu3-4|Pt} = \frac{G_{\uparrow\downarrow}}{G_{sh}}$ at the Co|Cu|Pt interface $\mathcal{T}_{\uparrow\downarrow}^{Co|Cu|Pt} = 0.55 \pm 0.05$.
- spin-mixing transmission $\mathcal{T}_{\uparrow\downarrow}^{Co|Al1.4|Pt} = \frac{G_{\uparrow\downarrow}}{G_{sh}}$ at the Co|Al(1.4)|Pt interfaces $\mathcal{T}_{\uparrow\downarrow}^{Co|Al(1.4)|Pt} = 0.2 \pm 0.05$.

The correspondence between the spin-mixing transmission $\uparrow\downarrow$ extracted from SOT and the electronic transmission \mathcal{T}_{σ} in the collinear magnetic configuration extracted from AHE measurements (spin and local magnetization are here

collinear) may be expressed as:

$$\frac{1}{\mathcal{T}_{\uparrow\downarrow}} \cong \frac{1}{2} \sum_{\sigma} \left(\frac{1}{\mathcal{T}_{\sigma}} \right) \quad (30)$$

for a single interface and:

$$\frac{1}{\mathcal{T}_{\uparrow\downarrow}} \cong \frac{1}{2} \sum_{\sigma}^{n=1..N} \left(\frac{1}{\mathcal{T}_{\sigma}^{(n)}} \right) + 1 - N \quad (31)$$

for N consecutive interfaces (n) e.g played by Co/Al/Pt.

- spin memory loss parameter at Pt|Co and Co|Cu|Pt interfaces [21, 26] : $\delta = 0.6$ (spin loss : $\tilde{\mathcal{L}} = 1 - \exp(-\delta) \approx 0.5$).

For Co|Al|Pt and Co|Cu|Pt interfaces, the spin-resistance of (Al,Cu)|Pt bilayers is needed. The spin-resistance of a two-consecutive layer spin-resistance with $\tilde{t} = \frac{t}{\lambda_{sf}}$ the ratio of the thickness over the Spin-Diffusion Length (SDL) of the spacer material considered: either Al or Cu, equals $r_s = r_s^{(1)} \frac{r_s^{(2)} \cosh(\tilde{t}) + r_s^{(1)} \sinh(\tilde{t})}{r_s^{(1)} \cosh(\tilde{t}) + r_s^{(2)} \sinh(\tilde{t})}$ where $r_s^{(1)}$ is the spin-resistance of the spacer (Al or Cu) and $r_s^{(2)}$ the spin-resistance of Pt. In the present case, the large spin-resistance of Al or Cu $r_s^{(1)}$ makes $r_s \approx r_s^{(2)}$.

In Fig. S12, we display the typical coordinate dependence in z of the two components of the spin-accumulation injected by SHE in the 5 nm thick ferromagnetic Co layer and transverse to the local $3d$ magnetization \mathcal{M} : *respectively* the FL and DL components are represented in blue and red color. These two components oscillates out-of-phase by precession in the exchange field of \mathcal{M} before attenuating by decoherence effects [27]. The calculation presented in Fig. S12 is performed for a Pt(8)|Co(5)|Al(1.4)|Pt(3) structure (a 5 nm thick Co layer was chosen here to exhibit the oscillatory dependence of the two torque components) and shows typical oscillating features like proposed in Refs. [12, 15].

D. The Rashba-Edelstein effect

The previous development mainly developed for the SHE component also holds for ultrathin ferromagnetic layers. In order to fit the experimental results, we have added an imaginary part to the local spin-density integrated within the thickness t_{Co} of the ferromagnetic layer and thus giving rise to a FLT component.

In the case of Pt(8)|Co(t_{Co})|Al(1.4 nm)|Pt(3), the resulting integrated FLT from REE for $t_{Co} > 0.5$ is set to $\tau_{SOT}^{FL} = 0.55 \exp[-q_{REE} (t_{Co} - 0.5)^2]$ with $q_{REE} = 0.7$ nm that represents 75% of the total FLT component in the $t_{Co} = 0.5 - 1.1$ nm range.

In the case of Pt(8)|Co(t_{Co})|Cu(1.4 nm)|Pt(3), the resulting integrated FLT from REE for $t_{Co} > 0.4$ is set to a constant, $\tau_{SOT}^{FL} = 0.2$, that represents 45% of the total FLT component for $t_{Co} = 0.5$ nm.

REFERENCES

-
- [1] S. Krishnia, E. Haltz, L. Berges, L. Aballe, M. Foerster, L. Bocher, R. Weil, A. Thiaville, J. a. Sampaio, and A. Mougin, Spin-orbit coupling in single-layer ferrimagnets: Direct observation of spin-orbit torques and chiral spin textures, *Phys. Rev. Applied* **16**, 024040 (2021).
 - [2] A. Ghosh, S. Auffret, U. Ebels, and W. E. Bailey, Penetration depth of transverse spin current in ultrathin ferromagnets, *Phys. Rev. Lett.* **109**, 127202 (2012).
 - [3] T. Taniguchi, S. Yakata, H. Imamura, and Y. Ando, Penetration depth of transverse spin current in ferromagnetic metals, *IEEE Transactions on Magnetics* **44**, 2636 (2008).

- [4] T. H. Dang, Q. Barbedienne, D. Q. To, E. Rongione, N. Reyren, F. Godel, S. Collin, J. M. George, and H. Jaffrès, Anomalous hall effect in 3d/5d multilayers mediated by interface scattering and nonlocal spin conductivity, *Phys. Rev. B* **102**, 144405 (2020).
- [5] D. A. Stewart, W. H. Butler, X.-G. Zhang, and V. F. Los, Interfacial scattering in magnetic multilayers and spin valves, *Phys. Rev. B* **68**, 014433 (2003).
- [6] J. Sinova, S. O. Valenzuela, J. Wunderlich, C. H. Back, and T. Jungwirth, Spin hall effects, *Rev. Mod. Phys.* **87**, 1213 (2015).
- [7] L. Liu, C.-F. Pai, Y. Li, H. W. Tseng, D. C. Ralph, and R. A. Buhrman, Spin-torque switching with the giant spin hall effect of tantalum, *Science* **336**, 555 (2012).
- [8] L. Liu, O. J. Lee, T. J. Gudmundsen, D. C. Ralph, and R. A. Buhrman, Current-induced switching of perpendicularly magnetized magnetic layers using spin torque from the spin hall effect, *Phys. Rev. Lett.* **109**, 096602 (2012).
- [9] K. Garello, I. M. Miron, C. O. Avci, F. Freimuth, Y. Mokrousov, S. Blügel, S. Auffret, O. Boulle, G. Gaudin, and P. Gambardella, Symmetry and magnitude of spin-orbit torques in ferromagnetic heterostructures, *Nature Nanotechnology* **8**, 587 (2013).
- [10] Y. A. Bychkov and É. I. Rashba, Properties of a 2D electron gas with lifted spectral degeneracy, *Soviet Journal of Experimental and Theoretical Physics Letters* **39**, 78 (1984).
- [11] S. Zhang, P. M. Levy, and A. Fert, Mechanisms of spin-polarized current-driven magnetization switching, *Phys. Rev. Lett.* **88**, 236601 (2002).
- [12] C. Petitjean, D. Luc, and X. Waintal, Unified drift-diffusion theory for transverse spin currents in spin valves, domain walls, and other textured magnets, *Phys. Rev. Lett.* **109**, 117204 (2012).
- [13] R. V. Shchelushkin and A. Brataas, Spin hall effect, hall effect, and spin precession in diffusive normal metals, *Phys. Rev. B* **72**, 073110 (2005).
- [14] V. P. Amin and M. D. Stiles, Spin transport at interfaces with spin-orbit coupling: Phenomenology, *Phys. Rev. B* **94**, 104420 (2016).
- [15] A. Kalitsov, I. Theodonis, N. Kioussis, M. Chshiev, W. H. Butler, and A. Vedyayev, Spin-polarized current-induced torque in magnetic tunnel junctions, *Journal of Applied Physics* **99**, 08G501 (2006).
- [16] B. K. Nikolić, K. Dolui, M. D. Petrović, P. Plecháč, T. Markussen, and K. Stokbro, First-principles quantum transport modeling of spin-transfer and spin-orbit torques in magnetic multilayers, in *Handbook of Materials Modeling: Applications: Current and Emerging Materials*, edited by W. Andreoni and S. Yip (Springer International Publishing, Cham, 2018) pp. 1–35.
- [17] A. Brataas, G. E. Bauer, and P. J. Kelly, Non-collinear magnetoelectronics, *Physics Reports* **427**, 157 (2006).
- [18] M. Cosset-Chéneau, L. Vila, G. Zahnd, D. Gusakova, V. T. Pham, C. Grèzes, X. Waintal, A. Marty, H. Jaffrès, and J.-P. Attané, Measurement of the spin absorption anisotropy in lateral spin valves, *Phys. Rev. Lett.* **126**, 027201 (2021).
- [19] M. D. Stiles and A. Zangwill, Anatomy of spin-transfer torque, *Phys. Rev. B* **66**, 014407 (2002).
- [20] T. Jungwirth, J. Wunderlich, V. Novák, K. Olejník, B. L. Gallagher, R. P. Campion, K. W. Edmonds, A. W. Rushforth, A. J. Ferguson, and P. Němec, Spin-dependent phenomena and device concepts explored in (ga,mn)as, *Rev. Mod. Phys.* **86**, 855 (2014).
- [21] J.-C. Rojas-Sánchez, N. Reyren, P. Laczkowski, W. Savero, J.-P. Attané, C. Deranlot, M. Jamet, J.-M. George, L. Vila, and H. Jaffrès, Spin pumping and inverse spin hall effect in platinum: The essential role of spin-memory loss at metallic interfaces, *Phys. Rev. Lett.* **112**, 106602 (2014).
- [22] I. Turek, V. Drchal, J. Kudrnovský, M. Šob, and P. Weinberger, Green function method, in *Electronic Structure of Disordered Alloys, Surfaces and Interfaces* (Springer US, Boston, MA, 1997) pp. 59–112.
- [23] A. Gonis and W. H. Butler, Formal development of mst, in *Multiple Scattering in Solids* (Springer New York, New York, NY, 2000) pp. 55–79.
- [24] T. H. Dang, J. Hawecker, E. Rongione, G. Baez Flores, D. Q. To, J. C. Rojas-Sanchez, H. Nong, J. Mangeney, J. Tignon, F. Godel, S. Collin, P. Seneor, M. Bibes, A. Fert, M. Anane, J.-M. George, L. Vila, M. Cosset-Cheneau, D. Dolfi, R. Lebrun, P. Bortolotti, K. Belashchenko, S. Dhillon, and H. Jaffrès, Ultrafast spin-currents and charge conversion at 3d-5d interfaces probed by time-domain terahertz spectroscopy, *Applied Physics Reviews* **7**, 041409 (2020).
- [25] V. P. Zhukov, E. V. Chulkov, and P. M. Echenique, Lifetimes and inelastic mean free path of low-energy excited electrons in fe, ni, pt, and au: Ab initio GW + T calculations, *Phys. Rev. B* **73**, 125105 (2006).
- [26] G. G. B. Flores, A. A. Kovalev, M. van Schilfgaarde, and K. D. Belashchenko, Generalized magnetoelectronic circuit theory and spin relaxation at interfaces in magnetic multilayers, *Phys. Rev. B* **101**, 224405 (2020).
- [27] K.-W. Kim, Spin transparency for the interface of an ultrathin magnet within the spin dephasing length, *Phys. Rev. B* **99**, 224415 (2019).